university of groningen

University Medical Center Groningen

University of Groningen

Complex Field Mapping of Large Direct Detector Focal Plane Arrays

Davis, Kristina K.; Yates, Stephen J. C.; Jellema, Willem; Groppi, Christopher E.; Baselmans, Jochem J. A.; Kohno, Kotaro; Baryshev, Andrey M.

Published in:
Ieee transactions on terahertz science and technology

DOI:
10.1109/TTHZ.2018.2883820

IMPORTANT NOTE: You are advised to consult the publisher's version (publisher's PDF) if you wish to cite from it. Please check the document version below.

Document Version
Publisher's PDF, also known as Version of record

Publication date:
2019

Link to publication in University of Groningen/UMCG research database

Citation for published version (APA):
Davis, K. K., Yates, S. J. C., Jellema, W., Groppi, C. E., Baselmans, J. J. A., Kohno, K., & Baryshev, A. M. (2019). Complex Field Mapping of Large Direct Detector Focal Plane Arrays. *Ieee transactions on terahertz science and technology*, *9*(1), 67-77. https://doi.org/10.1109/TTHZ.2018.2883820

Copyright
Other than for strictly personal use, it is not permitted to download or to forward/distribute the text or part of it without the consent of the author(s) and/or copyright holder(s), unless the work is under an open content license (like Creative Commons).

The publication may also be distributed here under the terms of Article 25fa of the Dutch Copyright Act, indicated by the "Taverne" license. More information can be found on the University of Groningen website: https://www.rug.nl/library/open-access/self-archiving-pure/taverne-amendment.

Take-down policy
If you believe that this document breaches copyright please contact us providing details, and we will remove access to the work immediately and investigate your claim.

Downloaded from the University of Groningen/UMCG research database (Pure): http://www.rug.nl/research/portal. For technical reasons the number of authors shown on this cover page is limited to 10 maximum.

Download date: 05-05-2023

Complex Field Mapping of Large Direct Detector Focal Plane Arrays

Kristina K. Davis, Stephen J. C. Yates, Willem Jellema, Christopher E. Groppi, Jochem J. A. Baselmans, Kotaro Kohno, and Andrey M. Baryshev

***Abstract*—Complex field mapping is a powerful tool to characterize the optical performance of astronomical instruments, and has become the standard for characterizing heterodyne array cameras. Recently, an adaptation of the heterodyne beam mapping technique was demonstrated on a single pixel of a direct detector instrument. We present a novel measurement apparatus and data acquisition techniques to efficiently reconstruct the complex field pattern of individual pixels across a direct detector focal plane array. These techniques are scalable to high pixel counts as the technology maturation and scientific requirements push to larger arrays. For this demonstration, we used an engineering model of the low-frequency band of the APEX microwave kinetic inductance detector camera with a center frequency of $\nu = 350$ GHz. Amplitude and phase radiation patterns were measured from all 880 pixels of the test array in two orthogonal polarizations. We also discuss an updated postprocessing pipeline using the complex field data to characterize the optical performance of the array. Using the measured complex field pattern, we extract the co- and cross-polarization patterns and Gaussian beam parameters, and propagate the beam from the measurement plane to additional planes of interest across all pixels in the test array. Complex field measurements of direct detectors allow more precise characterization of beam parameters when compared to thermal measurements, particularly for individualized fitting in postprocessing not reliant on the accuracy of the probe system alignment. These techniques enable high-precision characterization of individualized beam parameters as well as the overall optical system to very large format arrays with modest computational processing power. These results demonstrate the diagnostic power of the presented measurement and analysis techniques.**

***Index Terms*—Complex field mapping, Gaussian beam analysis, kinetic inductance detector, near-to-far-field transformation, optical characterization.**

I. Introduction

ASTRONOMICAL survey instruments naturally progress toward large focal plane cameras with wide-field optical schemes. Visible light cameras have achieved pixel counts in the hundreds of megapixels or more. At lower frequencies, both microwave kinetic inductance detector (MKID) [1]–[4] and transition-edge sensor [5]–[7] array cameras are being developed and are reaching kilopixel detector counts. Some of the next big scientific questions can be addressed with wide-field instruments, but require breakthroughs in sensitivity and polarization accuracy.

For example, the next generation of cosmic microwave background (CMB) mapping missions envisioned for both ground-based CMB Stage 4 (CMB-S4) and space-based CMB-S4 need unprecedented pointing knowledge, sensitivity, and polarization selectivity to detect or set limits on the energy in primordial B-modes of CMB photon polarization [8]. For imaging instruments studying extended sources, such as the polarization of thermal emission from dusty molecular clouds as the grains align to the galactic field lines [9], [10], accurate knowledge of the sidelobe structure of the beams is necessary for image reconstruction. As the field of view increases, it becomes difficult to ensure uniform alignment accuracy, stability, and coupling to calibration sources when characterizing the instrument prior to deployment. New characterization techniques are called for to address these scientific questions [11, Sec. 3.7].

Broadband (direct) detectors are phase insensitive, so the full on-sky beam patterns have traditionally been measured with thermal (incoherent) sources [12], typically in the far field of the instrument. However, complex (coherent) field mapping of both amplitude and phase patterns offers several advantages not available to thermal beam scans [13]–[16]. Coherent beam pattern measurements are standard for missions using heterodyne receivers, and have been used to characterize

Manuscript received August 31, 2018; revised November 11, 2018 and November 15, 2018; accepted November 16, 2018. Date of publication November 28, 2018; date of current version January 9, 2019. This work was supported in part by the ERC under Grant ERC-2009-StG and under Grant 240602 TFPA. The work of K. K. Davis was supported in part by the NSF Astronomy and Astrophysics Postdoctoral Fellowship under Award AST-1801983, in part by NOVA and the University of Groningen (for travel), and in part by Arizona State University. The work of J. J. A. Baselmans was supported by the ERC consolidator under Grant COG 648135 MOSAIC. *(Corresponding author: Kristina K. Davis.)*

K. K. Davis is with the Department of Physics, University of California at Santa Barbara, Santa Barbara, CA 93106 USA (e-mail: daviskk44@gmail.com).

S. J. C. Yates is with SRON Netherlands Institute for Space Research, 9700 AV Groningen, The Netherlands (e-mail: S.Yates@sron.nl).

W. Jellema is with SRON Netherlands Institute for Space Research, 9700 AV Groningen, The Netherlands, the Department of Science and Engineering, RUG, 9747 AD Groningen, The Netherlands, and also with the Kapteyn Astronomical Institute, University of Groningen, 9700 AV Groningen, The Netherlands (e-mail: w.jellema@sron.nl).

C. E. Groppi is with the School of Earth and Space Exploration, Arizona State University, Tempe AZ 85287 USA (e-mail: cgroppi@asu.edu).

J. J. A. Baselmans is with SRON Netherlands Institute for Space Research, 3584 CA Utrecht, The Netherlands, and also with the Terahertz Sensing Group, Faculty of Electrical Engineering, Mathematics and Computer Science, Delft University of Technology, 2628 CD Delft, The Netherlands (e-mail: J.Baselmans@sron.nl).

K. Kohno is with the Institute of Astronomy, University of Tokyo, Tokyo 181-0015, Japan (e-mail: kkohno@ioa.s.u-tokyo.ac.jp).

A. M. Baryshev is with the Kapteyn Astronomical Institute, University of Groningen, 9700 AV Groningen, The Netherlands (e-mail: andrey@astro.rug.nl).

Color versions of one or more of the figures in this paper are available online at http://ieeexplore.ieee.org.

Digital Object Identifier 10.1109/TTHZ.2018.2883820

2156-342X © 2018 IEEE. Translations and content mining are permitted for academic research only. Personal use is also permitted, but republication/redistribution requires IEEE permission. See http://www.ieee.org/publications_standards/publications/rights/index.html for more information.

instrumentation from small, ground-based missions to the large and satellite-class missions, such as IRAM, Herschel, ALMA, and others [15], [17]–[20].

A two-source coherent detection approach to beam characterization of direct-detector instruments in the submillimeter regime was first presented in [21] where the phase difference between the two sources was modulated to create interference fringes detected by a commercial power meter. An alternate approach was presented in [22] using a quasi-heterodyne technique where the two coherent sources are coupled in front of the instrument with a passive beamsplitter. The two sources are slightly offset in frequency, and the optical difference or "beat" frequency modulates the detector response in the time domain. By tuning the beat frequency to fall within the response time of the read-out system, the complex field parameters can be acquired through a fast Fourier transform (FFT) of the time-domain detector response signal. The beam map is created from the resulting amplitude and phase of the FFT peak as a function of source probe position.

Because direct detectors are not true mixing devices, the phase of the incoming signal is not preserved through the read-out system. Therefore, to properly reconstruct the phase pattern of the measurement, the detector response must be referenced to the drive signal in postprocessing in order to calibrate the optical-path phase delay. The reference tone is produced by splitting the drive signal at low frequency and passing one branch from each source to a low-frequency harmonic mixer. This technique is demonstrated with large antenna-coupled MKID arrays, but the technique can be generalized to any direct detector array, provided it has a sufficiently fast response time.

II. Methods

The work presented in [22] demonstrated detailed analysis on only a single pixel of a 3 × 3 array. Several modifications to the experimental apparatus, system configuration, and analysis pipeline were needed to efficiently scale the measurement system to large FPAs. First, a new optical injection scheme was necessary to uniformly illuminate the array with the local oscillator (LO) source. Instead of triggering data acquisition, we implemented continuous phase referencing by monitoring a modulated calibration tone in the multiplexed read-out system. We also used an on-the-fly (OTF) scanning strategy in order to minimize the scan duration as compared to a step-and-integrate scan strategy.

We also demonstrate an additional processing step in the analysis pipeline to extract the co- and cross-polarization radiation patterns from the measurement data. We took two scans in orthogonal directions that were at an arbitrary rotation angle with respect to the image plane. The co- and cross-polarization fields can be extracted individually for each pixel by reprojecting the two measurement planes onto a rotated coordinate system until the signal in the co-polarization field is maximized (and the signal in the cross-polarization field is minimized). Fitting the rotation angle allowed us to choose a scan axis orientation convenient for the laboratory scanning system rather than along the co- and cross-polarization axes of the image plane, which was rotated with respect to the optical bench. This characterization step produces highly accurate results of cross-polarization contamination for single-polarization detectors, and has the potential to accurately characterize polarization selectivity of dual-polarization detectors. We aim to address the characterization improvements called for in [11].

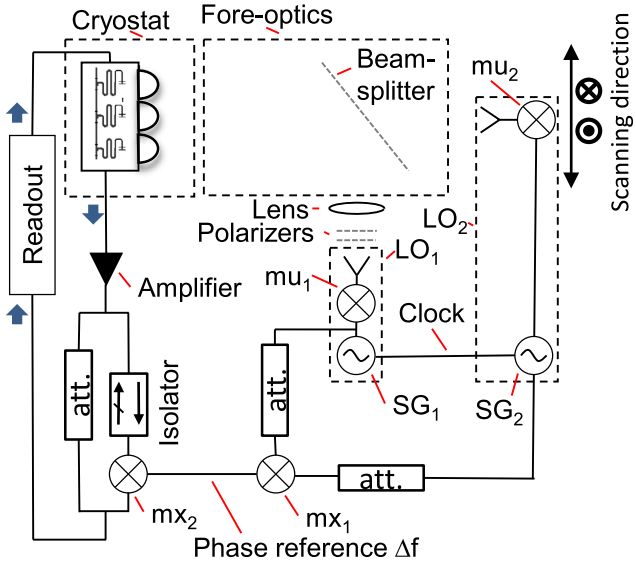

Fig. 1. Electrical and optical coupling scheme. The measurement measures the optical beating of two signals, from the LOs, one which is fixed and illuminates the entire array (LO_1) and other one which scanned (LO_2). Table I summarizes the frequencies at each step in the multiplication chain, reference tone, and read-out tones. The signal generators use a common 10-MHz clock. The power and polarization of LO_1 is controlled via two polarizers, and a 150-mm focal length lens is used to optimize the coupling over the field of view. The phase reference is generated separately by mixing the signal generators together, which is mixed with the MKID readout.

A. Signal-to-Noise and Dynamic Range

Phase patterns of direct detectors can be measured by modulating the detector readout in the time domain, and phase referencing the detector response to the optical modulation. Detector modulation is achieved by using the interference of two coherent radio frequency (RF) sources, as shown in Fig. 1. In this experiment, the RF signals are generated using a multiplier chain (LO_1) and a harmonic mixer (LO_2). Each multiplication chain ($mu_{1,2}$) outputs a signal at the Mth $= 32$nd harmonic of the drive signal.

The two synthesizers are driven with a small offset frequency (Δf), which produces a modulation frequency $\mathrm{IF}_{\mathrm{mod}}$ through coherent modulation of the quasi-particle number in the MKID pixel. At each point in the scan plane, ignoring higher order terms, the optical modulation of the stationary LO_1 and moving source probe LO_2 will modulate the power response of the detector according to

$$P_{\mathrm{det}}(x,y,t) \approx \frac{|\vec{E}_{\mathrm{LO}_1}|^2}{2} + \frac{|\vec{E}_{\mathrm{LO}_2}|^2}{2} + |\vec{E}_{\mathrm{LO}_1}||\vec{E}_{\mathrm{LO}_2}| \times \cos(2\pi M \Delta f t + \Delta\phi) \quad (1)$$

where $\vec{E}_{\mathrm{LO}_i}$ is the E-field generated by each of the two sources. Here, the $\vec{E}_{\mathrm{LO}_2}$ field represents the convolution between the source probe and the optical system's radiation pattern at each

TABLE I
SYSTEM FREQUENCIES

Component	Frequency
Signal Generator (SG_1)	11.25 GHz
Local Oscillator LO_1 ($SG_1 \times M$)	360.00 GHz
Signal Generator (SG_2)	11.25 GHz + 17.66 Hz
Source Probe LO_2 ($SG_2 \times M$)	360.00 GHz + 565.33 Hz
Offset Frequency (Δf)	17.66 Hz
IF_{mod} ($\Delta f \times M$)	565.33 Hz
Read-out Frequency Comb	4... 8 GHz + 17.66 Hz
M (multiplication factor)	32

Note: List of the frequencies of different components of the measurement system shown in Fig. 1.

point in the scan plane. LO_1 launches the radiation using a diagonal horn, and LO_2 uses an open-ended waveguide. In principle, complex field measurements allow for proper source probe deconvolution from the measured beam pattern though we skipped this step for this proof-of-concept demonstration.

The first two terms of (1) correspond to DC offsets, from direct coupling of the sources to the detector. A traditional amplitude-only optically chopped single-source measurement is represented by the second term, so the power signal detected P_{det} is proportional to the power of the beam pattern or $|\vec{E}_{\text{LO}_2}|^2$. The last term describes the optical modulation due to the coherent interference of the two sources, and so is used to extract the phase ($\Delta\phi$) and amplitude ($|\vec{E}_{\text{LO}_2}|$) beam pattern response. Note, in this case, P_{det} is proportional to the amplitude of beam pattern, $|\vec{E}_{\text{LO}_2}|$. This has the effect of squaring the dynamic range of the complex-field measurement compared to an amplitude-only measurement using a switched single optical source with the same source power, which is synchronously postdetected in the output. This enables us to achieve unprecedented signal-to-noise ratio for a direct detector instrument using the proposed method, with a (detector) noise floor of ~ -50 dB relative to beam maximum.

B. Phase Reference Generation

In order to efficiently scan the entire focal plane, we migrated away from a triggered to a continuous acquisition scheme, ultimately enabling OTF scanning and saving significant overhead. To create a continuous phase reference, we encoded the signal Δf onto the multiplexed MKID readout where it can be accessed as an additional effective pixel rather than a separate datastream. The phase reference signal was generated as in [22] by splitting a signal from the two drive synthesizers at low frequency and mixing the signals with a double-balanced mixer (mx_1), as can be seen in Fig. 1. The mixer was driven in the linear regime to accurately translate the reference and noise from the synthesizers while minimizing the higher order harmonic generation.

The read-out scheme of the array under test was based on a frequency domain multiplexing (FDM), where each MKID is coupled to a transmission line at an individual frequency in the range 4–8 GHz. A signal generator in the read-out system produces a frequency comb with a tone coupled to each MKID, plus an additional set of uncoupled tones called "blind tones." In normal operation, the blind tones are averaged together and then used to calibrate and remove electrical system drifts, phase delays, $1/f$ noise, and other instabilities [23].

Using a second double-balanced mixer (mx_2), we modulated the amplitude of the entire MKID read-out signal at Δf. The power in mx_2 was optimized to keep it in the linear regime, while an isolator was added in series to reduce reflections off mx_2 back to the signal generators. The phase reference was extracted from the modulated blind tones in data processing (described in Section II-D). Since the phase reference is at M times lower frequency than the optical signal, it was removed as a periodic system drift by the blind tone calibration. Therefore, there is no noise penalty for modulating the entire read-out signal, and we ensure there are no time delays or errors between the phase reference and data timestreams.

C. OTF Scanning Strategy

The beam mapping strategy used in [22] used a step-and-integrate scan mode. However, this strategy suffers from "dead time" as the scanner moves, and for wide-field instruments, this dead time can dominate the scan duration. We, therefore, adopted a partial OTF scanning strategy that proceeds as follows: At a given x position, the scanner is scanned slowly in y; then, moves to the next z position and repeats the y-scan (in order to remove optical standing waves in postprocessing); then, the scanner rapidly returns to a drift reference position (to enable long term drift removal); finally, the scanner moves to the next x position and repeats the process. A slow scan speed of 8 mm/s was used, so that each scan in y takes ~ 35 s. A crosscheck of the software trigger was performed by checking OTF and step-and-integrate beam pattern cross-cuts of the array.

D. Amplitude and Phase Extraction

The FDM readout of the array under test recorded a timestream from each MKID pixel at a rate of 1.272 kHz. The timestream was separated into "blocks" corresponding to the period of one full reference waveform (72 data samples or 56.6 ms). The speed of the OTF scan corresponds to a 0.11-s integration, equivalent to two reference waveforms (blocks) per 1-mm^2 scan plane coordinate. We perform a complex FFT of each block, and the output peaks in the frequency bin corresponding to the optical modulation IF_{mod}. An FFT of the phase reference signal (blind tone) at the same source probe location is performed, with the signal appearing in the bin corresponding to Δf. After recording the peak in the FFT of each signal, the phase of the reference signal is then multiplied by M and subtracted from the MKID phase. This produces the fully corrected complex field parameter at each x, y location in the scan plane.

Long term drifts in amplitude and phase of the system were measured by periodically returning to a reference position during the scan. The amplitude and phase at these reference measurements were interpolated and, then, subtracted from the interleaving points in the scan plane. First-order standing waves were removed from the measurement data by scanning the source probe by a quarter wave offset in z between two measurement planes, which were then averaged together according to [18] and [22].

III. Experimental System

A. Test Array

This demonstration of the complex field measurement technique was conducted using a representative wide-field, high pixel count, and direct detector array. Our choice was the AMKID, developed for the APEX telescope on the Atacama Plateau in Chile [24]. The AMKID array is separated into two frequency bands, with the higher band centered at $\nu = 850$ GHz. The low-frequency band (*L*-band) centered at $\nu = 350$ GHz is an 880-pixel single polarization MKID array with a $15' \times 15'$ field of view. Each frequency band consists of four MKID subarrays. One spare *L*-band subarray is characterized in this analysis.

Each individual pixel is a meandering MKID with a twin-slot coupling antenna. The pixels are hexagonally packed with a pitch of 2 mm on a chip measuring 60.8 mm $\times$ 62 mm. The antenna is fed by a silicon lens mounted to the front of the array. A stray light absorber is integrated into the chip to increase the imaging capabilities of the device. More details on the chip fabrication and results are presented in [25]. The dynamic range from the technique presented here was essential in identifying the mitigation of the on-chip stray light problem.

The test array was mounted at 250 mK in an optical cryostat designed to test subarrays for the A-MKID instrument. The wide-field optical system consisted of an aberration-compensated [26] optical relay of magnification $m = 3$ using four active mirrors and threefold mirrors. A cold aperture (pupil) limits the opening angle on the array to 14°, or a focal length to diameter (f#) ratio of 2 at the array. The band is selected by a bandpass filter, data presented here use one centered at 350 GHz. The source probe was scanned near the external focus of the warm optical system. At this plane, the array image size is 180 mm $\times$ 180 mm, which is slightly smaller than the FOV. GRASP simulations of the full end-to-end optical system predict a waist size of ≈ 3.25 mm in this focal plane [27]. More details on the cryostat and optics system are presented in [25] and [28].

B. LO Injection

To measure all pixels simultaneously, the static source LO_1 needs to be optically coupled to the entire array. However, with the folded optics there is not enough space to couple LO_1 at the image focal plane. This difficulty was solved by weakly coupling LO_1 with a thin-film beamsplitter at a position near the pupil image in the warm optics. The beamsplitter reflected $\lesssim 5\%$ of the beam into the optical path, and we ensured that the transmitted, nonreflected power from LO_1 (and reflected MKID beam) was terminated on a 300k load. A matching lens was used between the LO and beamsplitter but with an intentional defocus to allow coupling across the entire array. Additionally, two polarizers were added to fix the LO polarization and allow tunability of the source power. The absolute coupling of LO_1 power to each pixel varies across the array, but we normalized each beam to its peak power for further postprocessing. Therefore, the coupling factor calculated for each beam is a representative of the beams Gaussianity rather than absolute power coupling. As long as there is a sufficient signal-to-noise ratio at the individual pixel, the beam fitting algorithm will not be affected.

IV. Analysis

The analysis pipeline we created for the complex field maps described here can be broken into following three main stages:

1) extraction of the amplitude and phase information from the raw data timestream to a complex beam map via the FFT and phase referencing, as described in Section II-D;
2) preliminary map processing via performing a linearity analysis between the two polarized scan planes, the elimination of standing waves, and making co- and cross-polarization maps, described in Section IV-A;
3) optical analysis of the processed maps including Gaussian beam fitting, and beam propagation including a near-to-far-field transformation, described in Section IV-B.

A. Map Processing

1) Polarization: For either single or dual-polarization selective pixels, it is important to distinguish the co- and cross-polarization components of the beam pattern to accurately fit for the fundamental beam parameters. In principle, the co- and cross-polar beam patterns can be measured with only two scans taken at orthogonal polarizations of a singularly-polarized source probe, as discussed in [29]. This is generally true for both power-pattern and complex field measurements, though for power-pattern measurements, the source probe must be precisely aligned with each of the field components, which may be unknown. The advantage of complex field measurements is that the source probe can be aligned in any orientation with respect to the actual co- and cross-polarization axes of the detector beam, and can be fit for individual pixels rather than measured with respect to a mean coordinate system.

The radiation pattern of the FPA was measured twice at orthogonal orientations of the source probe, resulting in the measurements $\vec{E}_h$ (horizontal) and $\vec{E}_v$ (vertical). In the data presented here, the source was aligned close to the co-polarization orientation of the array for one scan and close to the cross polarization for the second scan. We keep the convention of the subscripts h and v to avoid confusion with the $\vec{E}_c$ (co-polar) and $\vec{E}_x$ (cross-polar) field maps.

In postprocessing, the measured fields can be projected onto arbitrary axes by the angle θ_{proj}, given in [29, eq. 8], and a minimization algorithm can be applied to solve for the transformation that minimizes power in the cross-polar field $|\vec{E}_x|$ [30]. The orthogonal field is, thus, the co-polar field component $\vec{E}_c$. Because the raw data maps were scanned over a large FOV relative to the individual beam size (as shown in Fig. 2) and include an elevated off-axis signal, we selected only an inner portion of the raw data to pass to the fitting routine.

In order to minimize $|\vec{E}_x|$, the amplitude centroid of the two maps $\vec{E}_h$ and $\vec{E}_v$ must be coaligned as accurately as possible. The raw data maps were gridded onto a 1-mm spacing, but this sampling was too coarse to see the fine detail of the cross-polarized maps. We linearly interpolated the data onto a

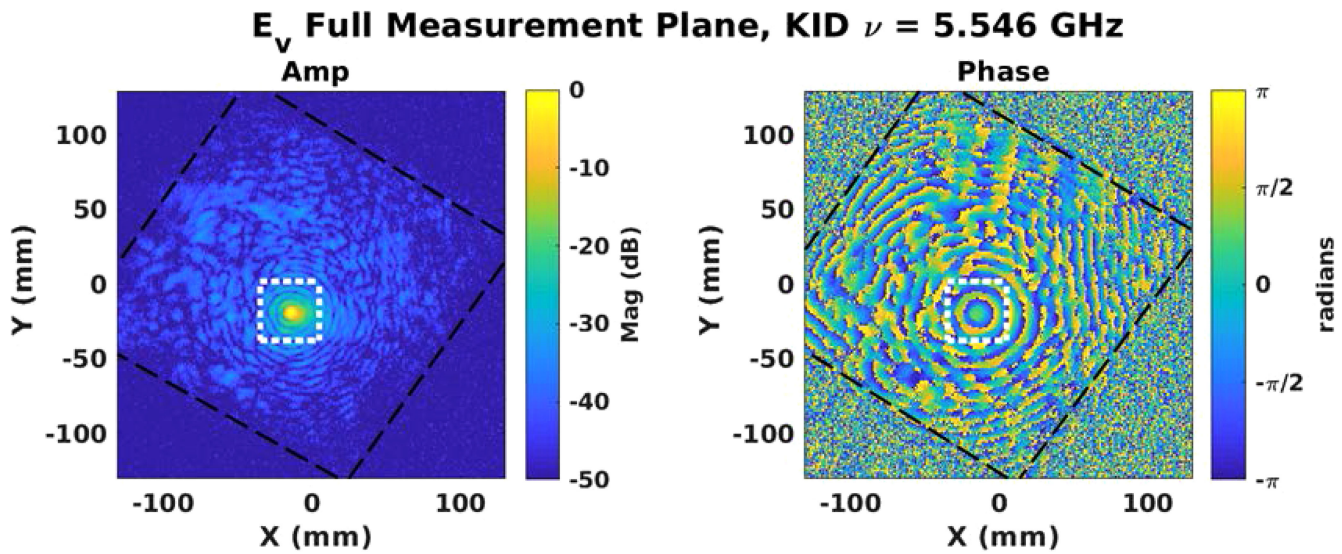

Fig. 2. Full preprocessed complex field map for a representative pixel located at the center of the array. The data are shown for the E_h polarization, and have not yet been processed to find the co- and cross-polarization axes. The long black dashed lines show the extent of the array before dropping off to the noise floor at ~ -50 dB. This highlights the rotation of the scan plane with respect to the instrument's principle $\hat{x}$ and $\hat{y}$ axes. The extent of the scan plane past the edges of the array was chosen to reach a -30 dB minimum in the radiation pattern of the edge pixels, and also to allow spatial filtering for the beam fitting and far-field transformation pipeline processes, described in Sections IV-B1 and IV-B2. The inner white dashed lines indicate the portion of the co-polar data that were sent to the beam fitting algorithm.

0.2-mm grid spacing and used a cross-correlation routine to find the amplitude centroid offset between the two map orientations. We then used a circular shift to coalign the two datasets.

Initially, a subset of 100 pixels in the center of the FPA was fed into the polarization algorithm using the range $-\frac{\pi}{2} < \theta_{\rm proj} < \frac{\pi}{2}$ with increments of $\frac{\pi}{180}$. Once the average projection angle was found, we ran the algorithm over the full array but narrowed the projection angle range to $-\frac{\pi}{6} < \theta_{\rm proj} < 0$ with increments of $\frac{\pi}{360}$. We find that the average rotation angle across the array is $\theta_{\rm proj} = -14.9 \pm 0.1^\circ$. Fig. 3 shows the resulting $\vec{E}_c$ and $\vec{E}_x$ fields of a central array pixel in both amplitude and phase. The cross-polar maximum was 21.3 $\pm$.9 dB below the co-polar field maximum on average across the array.

2) Linearity: To linearize the response of each MKID to the optical power, we compare each timestream to the relative frequency shift $(f - f_0)/f_0$, where f_0 is the MKID resonance frequency, which is linear to the detected optical power [31], using the procedure in [32]. We check this technique by decreasing the drive power to the source probe for several iterations of a linear cut across the measurement plane.

Because of the close alignment to the co- and cross-polarization axes, the power absorbed by the array during the $\vec{E}_h$ measurement was significantly stronger than during the $\vec{E}_v$ measurement. Using the results of the linearity check, we increased the drive power to the source probe by $+17.8$ dB for the $\vec{E}_v$ scan so that the detected power produced comparable signal-to-noise ratio in each map. For the polarization fitting, the scaling factor $Ae^{i\phi}$ from [29, eq. 8] assumes that the source probe power is equal between the two measurement scans. We, therefore, scaled $|\vec{E}_h|$ by $+17.8$ dB before fitting the values of A and ϕ. A encompasses the coupling difference between the source and detector at each orientation, and also adjusts for the relative power levels received by each individual pixel across the array.

3) KID Matching: As part of the automatic start-up routine, the KID frequencies are recalibrated between each measurement scan because the resonant frequency of each device can shift due to different thermal or optical loading conditions within the cryostat, as well as from changing the source probe drive power as mentioned earlier. The consequence of that step for this analysis was that the KID pixel read-out frequencies differ between the $\vec{E}_h$ and $\vec{E}_v$ scans, which must be frequency matched for further processing.

Therefore, a processing step was introduced to match individual pixels between the $\vec{E}_h$ and $\vec{E}_v$ datasets. We used a two-step matching technique that finds the closest match in frequency between the two scans but does a follow-up check on the location of the amplitude maximum. With an initial pixel count of 732 pixels, the routine matched 718 pixels corresponding to a matching yield of 98.1%.

B. Data Analysis

1) Beam Fitting: The beam fitting analysis routine used in our pipeline is a scaled version of that presented in [18] and [22] to fit a fundamental Gaussian beam to the measurement data. As can be seen in Figs. 2–4, there is a significant sidelobe structure in the beams of this test array, and this fit is only approximate. We could, in principle, recover different information about the optical system by fitting for a other beam functions, for example, a higher order Gaussian function or a first-order truncated two-dimensional (2-D) Bessel function [33], [34]. The framework presented here is easily adaptable to other fitting functions while maintaining an approximately equal degree of computer processing time.

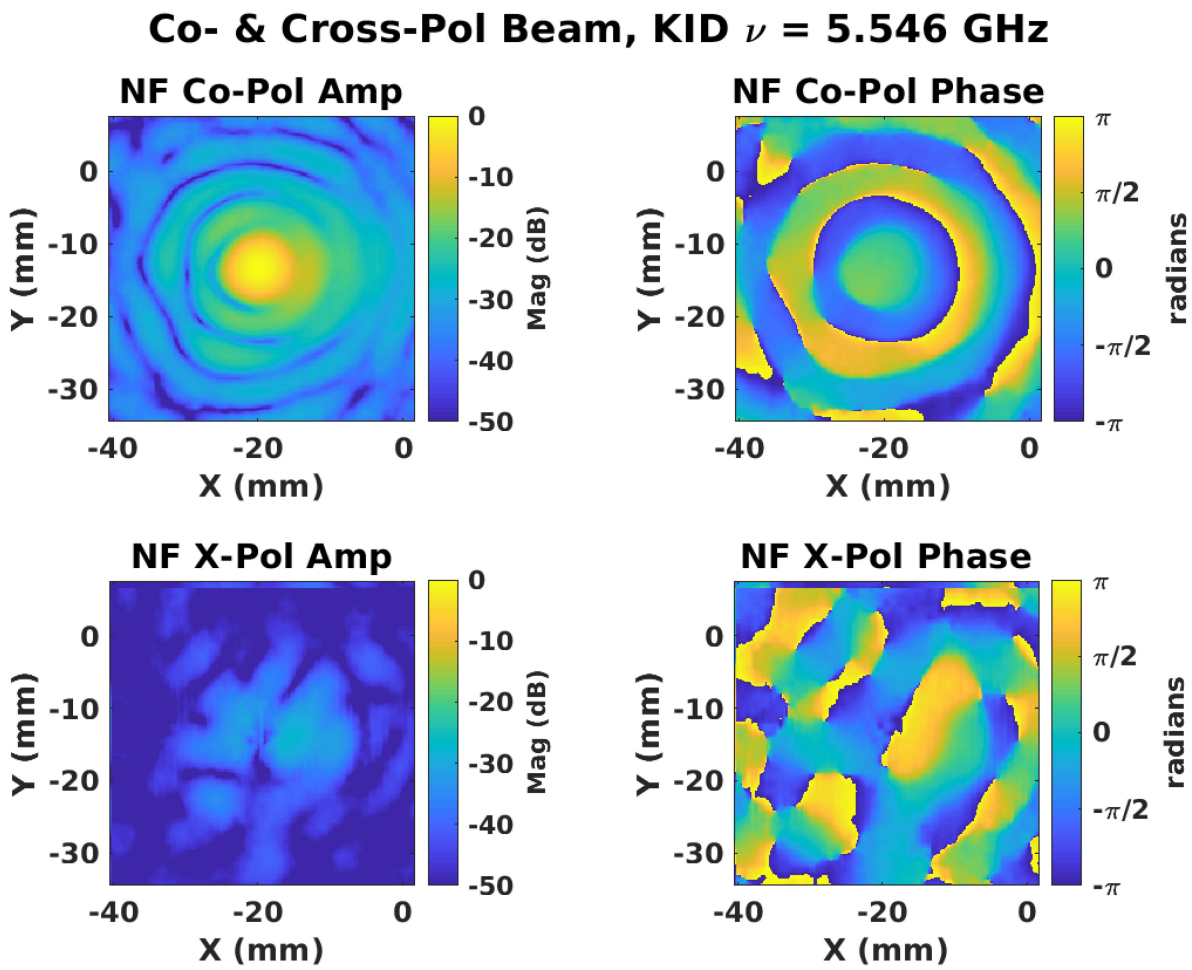

Fig. 3. Near-field co-polarization (upper two panels) and cross-polarization (bottom two panels) beam maps for the same representative pixel as shown in Fig. 2. The left two panels show the amplitude, scaled to the peak of the co-polarization map, and the right two panels show the phase structure. The image has been cropped to a square 8 × the beam width, centered on the amplitude peak in the co-polarized map to cut out the wide-field noise.

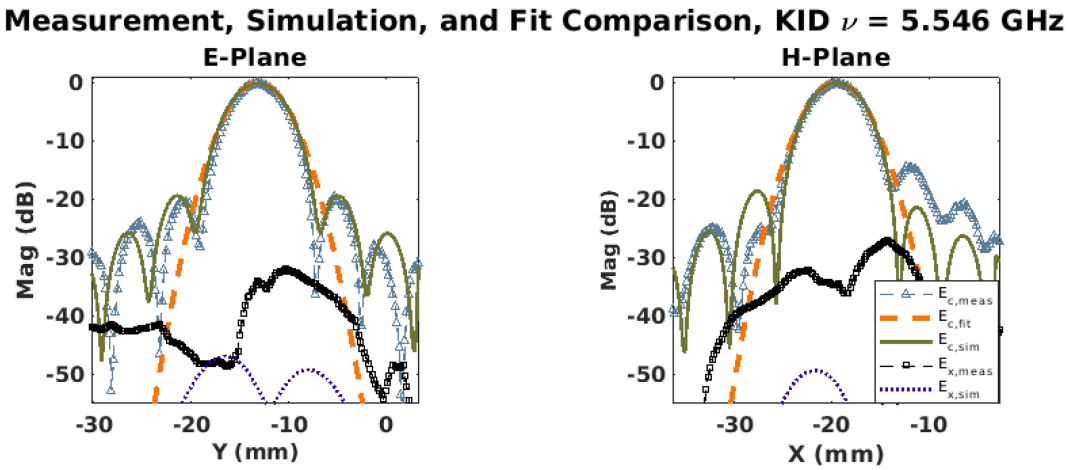

Fig. 4. Cuts in both the $\hat{E}$ (left) and $\hat{H}$ (right) planes of the near-field 2-D co-polarized beam patterns $E_{c,\mathrm{meas}}$ are projected back to the focal plane at $z = -33$ mm (see Section V). We also plot the results of the fitting function $E_{c,\mathrm{fit}}$, which is the first-order Gaussian function $|\psi_{00}|$, and the beam pattern cross-cuts from optical simulations $E_{c,\mathrm{sim}}$. The simulated patterns include the effects of the truncation of the beam on the secondary mirror and more fully simulate the optical properties of the receiver system. We see a strong null in the measured cross-polar pattern $E_{x,\mathrm{meas}}$, showing that we recover the cross-polar pattern after reprojection. However, the measured cross-polar peak is 15 dB higher than simulated $E_{x,\mathrm{sim}}$, caused by coupling to stray light both optically and in the device substrate, nonidealized optical components and slight alignment errors, and a small amount of coupling to the cross-polarization field of the source probe.

TABLE II
BEAM FITTING PARAMETERS AND FITS

Fitting Parameter	Simulation	Initial Guess Value	Average
$\omega_{o,x}$ (mm)	3.25	3.25	3.56±0.03
$\omega_{o,y}$ (mm)	3.25	3.25	3.54±0.03
x (mm)	–	x_{NFmax}	–
y (mm)	–	y_{NFmax}	–
z (mm)	–	-1.0	-33.7±0.6
θ_{TB1} (rad)	–	0.0	3.73±0.01 $*10^{-3}$
θ_{TB2} (rad)	–	0.0	4.97±0.01 $*10^{-3}$
θ_{TB3} (rad)	–	0.0	9± 3 $*10^{-3}$

Note: List of beam fitting parameters. The third column shows the value used to seed the initial minimization algorithm, and the right-most column shows the average fit values and standard deviation across the array. Only the values of $\omega_{o,x}$ and $\omega_{o,y}$ represent design parameters, and the lateral and rotational offsets $x, y, z, \theta_{\mathrm{TB1}}, \theta_{\mathrm{TB2}}$, and θ_{TB3} represent alignment errors between the probe system and image plane and are, therefore, included in the beam fitting parameters but are not derived from simulation results. The uncertainties listed here are the uncertainties for each parameter averaged across the array, and not the scatter in the values for each pixel.

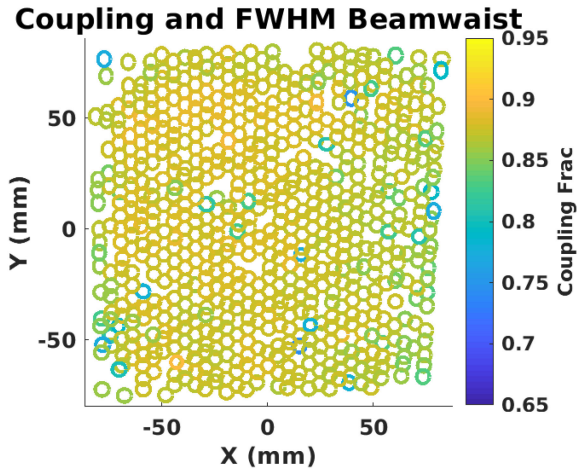

Fig. 5. This plot simultaneously shows the beam ellipticity and coupling coefficient for each pixel across the array. The shape of each beam is proportional to ω_x and ω_y at the distance z (focal plane) fit for each pixel according to the coordinate system transformation outlined in Section IV-B1. The color of each beam is proportional to the coupling value c_{00}. Not shown are pixels for which the beam fitting algorithm does not converge. Note that we have rotated the array footprint compared to the black box shown in Fig. 2.

The Gaussian beam fitting routine fits for the fundamental beam parameters $\omega_{o,x}$ and $\omega_{o,y}$ by creating a new coordinate system at location x, y, z and is rotated with respect to the scan plane by the Tait Bryan angles $\theta_{\mathrm{TB1}}, \theta_{\mathrm{TB2}}, \theta_{\mathrm{TB3}}$ from which to propagate an idealized, fundamental Gaussian beam ψ_{00}. A minimization function takes the set of initial seed parameters to define a fundamental Gaussian beam in a coordinate system relative to the focal plane, propagates the beam forward to the measurement plane, calculates the coupling loss coefficient between the measurement and fit data, and iterates over the parameter space until a convergence criterion is met.

The first pass of the beam fitting routine used an unbounded Nelder–Mead [30] minimization function, which efficiently probes the parameter space and has a low probability of converging to a local rather than global minima. The output parameters were passed as the initial guess for a second-pass beam fitting function, which used a nonlinear least-squares minimization function [35], which is also unbounded. The least-squares algorithm allowed us to more easily find the confidence intervals for the solution set of beam parameters. This is the most computationally expensive step in the analysis routine, but can be accomplished in a small number of hours depending on a number of analyzed pixels, closeness of the initial guesses, and hardware capabilities of the machine used for the analysis.

Table II presents the initial values used to seed the first-pass minimization algorithm, as well as the average of the final fit values for all 718 matched pixels. Initial parameters for the beam characteristics were taken from optical simulations using the parameters from lens-antenna simulations in CST [36], which were then ported into GRASP [27] for full end-to-end beam pattern simulation. The simulation data are included in Fig. 4, which compare amplitude crosscuts of the simulated beam pattern, the measured data $|E_c|$, as well as the magnitude of the idealized first-order Gaussian beam $|\psi_{00}|$ for a representative array pixel. We include the comparisons of the measured and simulated cross-polar patterns. Because we use a first-order Gauss–Hermite polynomial for fitting, we do not fit for sidelobes. We discuss the choice of fitting function in Section V.

Fig. 5 shows the coupling coefficient between the co-polar map and the first-order Gaussian beam. The shape of each pixel is representative of the beam's ellipticity. Optical simulations predict 91% coupling [37] to a fundamental Gaussian. We attribute the slight discrepancy between the simulation and measured Gaussicity to the remaining stray light scattering within the chip. We see no significant trend between coupling and pixel position, although we have eliminated pixels for which the beam fitting algorithm did not converge to a solution, which typically signifies crosstalk in the beam.

Initial testing of the beam fitting algorithm included a value to parameterize the beam's astigmatism, as presented in [22]. This value is the z offset between the phase centers in the x and y directions (parameter $\delta z_{x,y}$ as defined in [18]). However, when analyzing the beam fitting equation, we found that the function is fairly insensitive to the z parameter, where a 10 mm change in z produces only a $\sim 1\%$ change in the beam coupling. Upon further inspection, we found that the minimization function was oscillating between two minima for different values of z and $\delta z_{x,y}$; thus, these two parameters are not sufficiently independent for the level of noise present in this dataset. We removed this parameter from the fitting routine and kept the fit in z only. We still solve for the beam ellipticity by independently fitting the beam along the x and y axes, to find ω_x and ω_y.

Fig. 6 shows the value of the fit in z, effectively the distance of the measurement plane from the focal plane of the optical system, as a function of pixel position. The mean fit distance was -33 ± 6 mm. The sensitivity of the algorithm is only weakly coupled to the distance in z, and the ± 6 mm spread falls within the noise level. Though the spread is still large, we see no significant trend across the array.

2) Near-to-Far-Field Transformation: We took advantage of the external focus of the optical system to measure the complex beam pattern in the near field of the reimaged focal

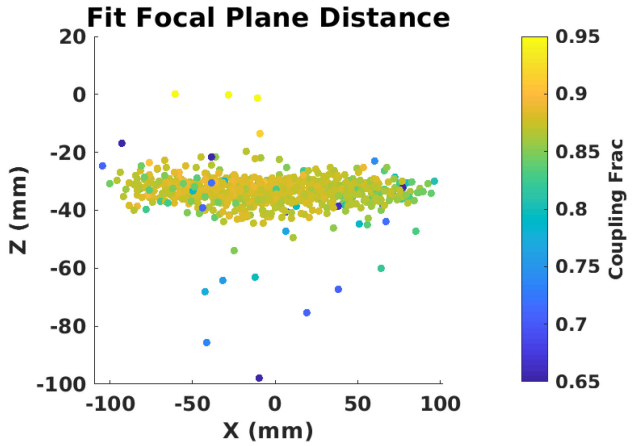

Fig. 6. Projection of the calculated distance to the focal plane for each pixel as viewed from the *XZ* plane. As in Fig. 5, the color of each pixel is related to the coupling percentage. Pixels with z fits outside the standard deviation of the focal plane distance tend to also have atypical coupling coefficients.

plane. At this plane, the confocal distance is $z_c = \pi {\omega_o}^2/\lambda = \pi 3.25^2/0.833 \approx 40$ mm [38]. We then solved for the far-field beam pattern following an angular plane wave spectrum technique [13], [39], which was accomplished with an FFT.

Instead of clipping the data in a boxed region as in Section IV-B1, we applied a circularly symmetric Hanning window function over the full 260 mm $\times$ 260 mm co-polar map. The windowing region was centered on the amplitude maximum and had a radius of $r_{\text{Hann}} = 24$ mm. Masking reduces the contribution from the noise floor outside the beam, as well as stray light "speckling" that arises from either the residual scattering inside the optics system [40] or from the residual stray light within the chip [25], not absorbed by the on-chip absorber. If the desire is to characterize the stray light performance of the array, the masking step can be skipped. Here, we use the filter mask to bring out the features of the cross-polar far-field map, which would otherwise be dominated by the stray-light noise.

The upper two panels of Fig. 7 show the far-field amplitude and phase of the co-polar field, and the bottom two panels show the amplitude and phase of the cross-polar field. Here, the phase pattern has been shifted by $E_{\text{ff}} = E_{\text{ff}} * \exp\left[i\left(k_x x_o + k_y y_o + k_z z\right)\right]$ to propagate from beam center rather than the center of the scan coordinates. The far-field pattern represents the illumination of the beams at the aperture stop of the optical system (i.e., the secondary mirror of the telescope). Though it appears mostly flat, the field in the central amplitude region of the co-polar far-field projection is a truncated Gaussian with an edge taper of $\gtrsim -5$ dB on average across the array due to the oversampling of the focal plane [41].

Once the phase correction was applied, we found the phase center in angular coordinates k_x, k_y by setting all coordinates of the co-polar map with amplitude > -10 dB to unity and nulling all coordinates with amplitude < -10 dB. We then averaged all the coordinates with signal to find the central coordinates of the beam, which corresponds to the boresight angle of each pixel fitted in the far field. Each pixel is shown with an arrow representing the boresight angle in Fig. 8, where the direction of each arrow is the representative of the boresight angle and the length is proportional to the magnitude in that direction.

V. Discussion

As a result of the complex field radiation pattern measurement, the AMKID array was measured with a dynamic range of $>$50 dB, a two to three orders of magnitude improvement over thermal beam scans of the same array. This dynamic range revealed the presence of a $-$ 30-dB optical surface wave in an early fabrication run of the AMKID array, which was removed by adding an absorbing mesh for subsequent fabrication runs [25]. The results we present here are measurements from an array fabricated with an absorbing mesh in the substrate. Our results show a decrease in the magnitude of the surface wave to $\lesssim -40$ dB, at a power level only easily measurable with the complex mapping technique that offers such a high dynamic range.

We summarize the trends in beam fitting parameters across the array in Fig. 9. The overall trend of the beam parameters, such as presented in Fig 9, can be used in conjunction with spatially correlated beam parameters, such as Fig. 5, to help diagnose individual errors likely caused during device fabrication from correlated errors likely arising from the optical system. It is even possible to propagate the beams backward or forward to the different optical planes in order to confirm these effects.

The far-field transformation in Section IV-B2 demonstrates the ability to measure the near-field beam pattern of direct detectors, which is possible from amplitude-only measurements but requires multiple measurement planes [42]. It is also worth noting that complex field measurements can be propagated and recreated at any distance from the measurement plane. We achieve this with a 2-D inverse FFT of the beam after propagating by a chosen value of $\pm z$. Beam propagation was used in Fig. 4, which compares the cross-cuts of the beam patterns at the focal plane, $-$ 33 mm from the measurement plane. Fig. 10 shows the 2-D beam patterns at the focal plane and at 100 mm from the measurement plane at the exit aperture position of the optics. The exit aperture is visible in the data as a rectangular truncation of the low-level stray light. We demonstrate that with this technique it is possible to check the illumination and alignment of the beams with respect to this aperture or any other major limiting apertures in the system.

The far-field co-polarized beam map confirmed the secondary edge taper of only $\sim -$ 5 dB, verifying the optical design of the system at planes other than the measurement plane. The results of both the near-field beam fitting and far-field radiation pattern confirms the fact that they are only somewhat Gaussian in nature, and the highly truncated beams are dominated by diffraction effects through the cold stop. The choice to fit for a Gaussian beam stems from the desire to know the coupling to a point source for each individual pixel. In this analysis with the AMKID array, the fundamental beam produced by the lenslet array was designed to produce more

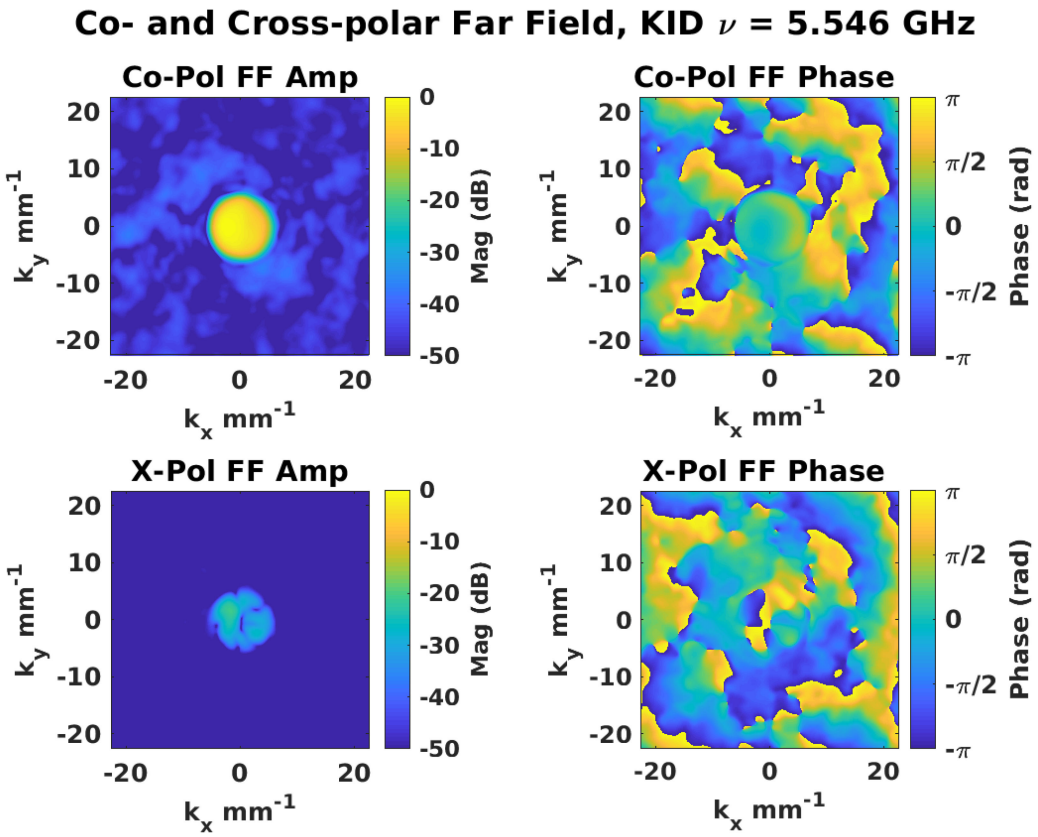

Fig. 7. Far-field radiation patterns of the representative MKID pixel. The upper two panels are the co-polar far field, lower two panels show the cross-polar far field. The left two panels are the amplitude patterns and the right two are the corrected phase patterns. We recover a null in the central region of the cross-polar amplitude map, demonstrating that we are able to fit for the proper cross-polarization field even at an elevated signal compared to the design.

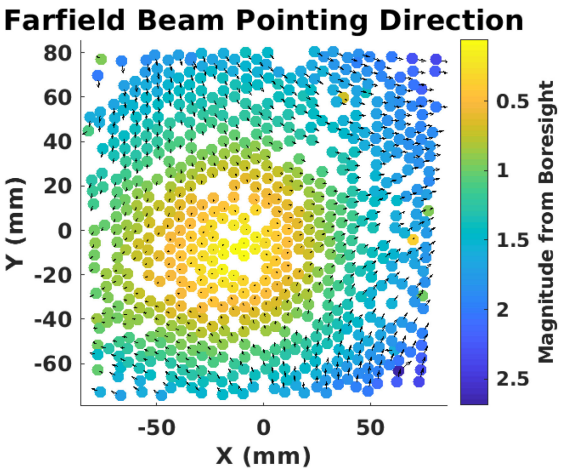

Fig. 8. Black arrows overlaid on the MKID pixels point in the direction of the boresight angle. The length of the arrow is proportional to the magnitude along the pointing direction, but scaled by a factor of 25 to be visible in this image. The color of each pixel is the representative of the magnitude of the difference between the pointing direction and boresight. Because the beams have to be scaled by a large factor to show the pointing direction, we demonstrate that overall the beams are very well aligned to the optical axis.

Gaussian beams, but the significant truncation at the pupil degrades the Gaussian coupling produced at the measurement plane.

The results of beam mapping for this array show an asymmetry in the first-order sidelobes of the beam, first appearing in the H-plane of the near-field pattern. This is seen also as the off-center midpoint in the amplitude and phase of the far-field pattern, and is most pronounced in the asymmetric phase of the cross-polar pattern. By analyzing the combined beam projections and removing the scan system misalignments during beam fitting, we conclude the error is caused by a misalignment in the cold optics, which may arise either from a misalignment of the lenslet [43] array or the cold stop. Amplitude-only near-field measurements would reveal only a sidelobe asymmetry, which can be difficult to interpret and are not as conclusive as complex field measurements.

This level of detailed analysis will be crucial to ascertain the accuracy of instrument fabrication when looking to the future of space missions using direct detectors with thousands to hundreds of thousands of pixels. For example, the next generation of CMB mapping satellites envisioned for CMB-S4 need unprecedented pointing knowledge to detect or set limits for the energy in primordial B-modes of CMB photon polarization. For imaging instruments studying extended sources, accurate pointing knowledge of the beams is necessary to fully reconstruct the source. The technique we present here is a highly accurate and efficient measurement of the co- and cross-polarization fields of an instrument and can be located at any scan plane convenient for *in situ* beam scanning.

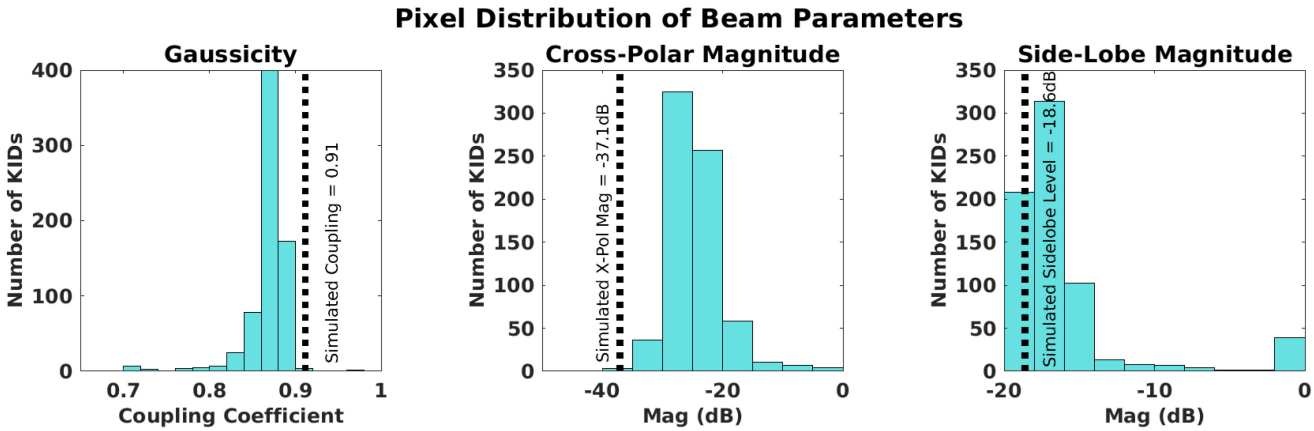

Fig. 9. Histograms of Gaussicity, sidelobe level, and maximum cross-polar level versus number of pixels across the array. We include the expected value as a dashed line taken from simulations of the co- and cross-polarized field data. To get the maximum sidelobe level from the 2-D co-polar data, we masked out the main beam and found the next highest peak. The pixels with a -5 to 0 dB sidelobe magnitude in that histogram are likely the number of pixels with crosstalk. For this particular array, we show slight variation between the measurement and simulated values for all three beam properties. The dominant reasons for this are 1) an optical misalignment leading to increased sidelobe level, 2) stray light from the optics and residual surface wave in the array, and 3) slight elevation of the cross-polarization level due to the cross polarization of the open-ended waveguide source probe.

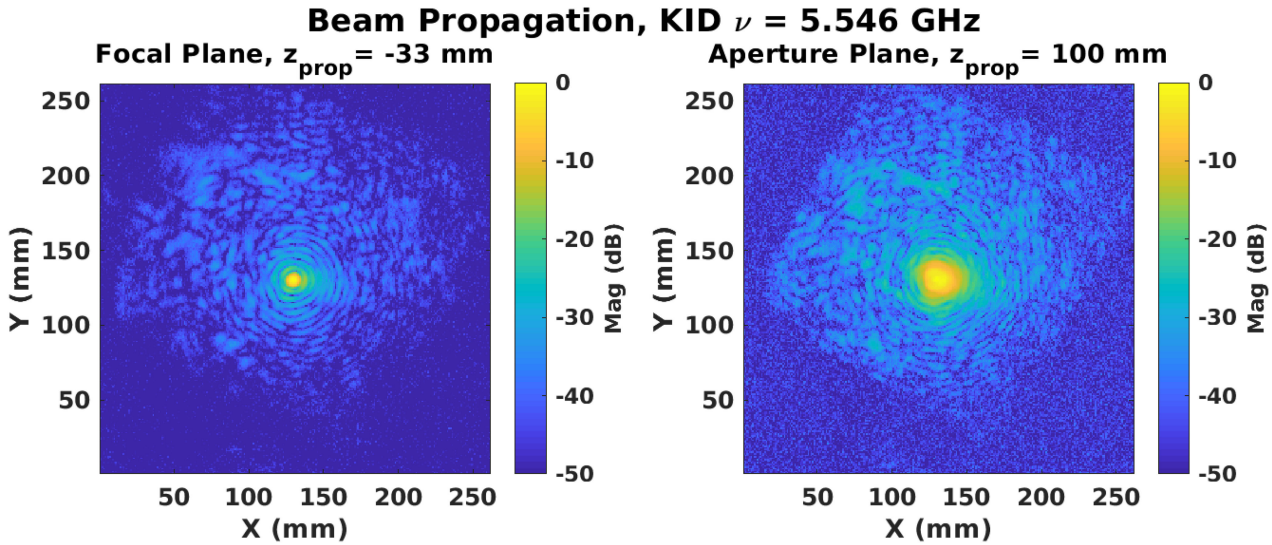

Fig. 10. Demonstration of propagating a beam from the focus position found during the beam fitting routine in Section IV-B1 at $z = -33$ mm (the fit waist position), and outward from the measurement plane at $z = 100$ mm (location of exit aperture of the warm optics). The choice of propagation distance aligns with the location of the pupil plane. In this demonstration, we propagate the beam from unmasked data in the measurement plane.

VI. Conclusion

A phase mapping technique for direct detector arrays was demonstrated with sufficient sensitivity and accuracy to determine fundamental beam parameters of the individual pixels as well as the optical performance of the system. New analysis techniques were included in a data reduction pipeline for beam pattern characterization of direct detector arrays, including extracting co- and cross-polarization maps from data scanned with an arbitrary source probe polarization orientation and near-to-far-field optical propagation.

Acknowledgment

First, the authors would like to thank R. Hesper for his contributions to the hardware optical system and software to run the motion stages. The authors would also like to thank O. Yurduseven and N. Llombart from the Delft University of Technology for work on the beam simulations of the array.

References

[1] P. K. Day, H. G. Leduc, B. A. Mazin, A. Vayonakis, and J. Zmuidzinas, "A broadband superconducting detector suitable for use in large arrays," *Nature*, vol. 425, no. 6960, pp. 817–821, Oct. 2003.

[2] J. J. A. Baselmans *et al.*, "A kilo-pixel imaging system for future space based far-infrared observatories using microwave kinetic inductance detectors," *Astron. Astrophys.*, vol. 601, 2017, Art. no. A89.

[3] S. Doyle, P. Mauskopf, J. Naylon, A. Porch, and C. Duncombe, "Lumped element kinetic inductance detectors," *J. Low Temp. Phys.*, vol. 151, no. 1/2 pt. 1, pp. 530–536, 2008.

[4] R. Adam *et al.*, "The NIKA2 large-field-of-view millimetre continuum camera for the 30 m IRAM telescope," *Astron. Astrophys.*, vol. 609, 2018, Art. no. A115.

[5] K. D. Irwin and G. C. Hilton, "Transition-edge sensors," *Topics Appl. Phys.*, vol. 99, pp. 63–149, 2005.
[6] R. W. Romani, A. J. Miller, B. Cabrera, E. Figueroa-Feliciano, and S. W. Nam, "First astronomical application of a cryogenic transition edge sensor spectrophotometer," *Astrophys. J.*, vol. 521, no. 2, pp. L153–L156, 1999.
[7] J. Beyer, "Transition edge sensor series array bolometer," *Superconductor Sci. Tech.*, vol. 23, no. 10, 2010, Art. no. 105019.
[8] K. N. Abazajian *et al.*, *CMB-S4 Science Book*, 1st ed., Oct. 2016. [Online]. Available: https://arxiv.org/abs/1610.02743
[9] N. Galitzki *et al.*, "The next generation BLAST experiment," *J. Astron. Instrum.*, vol. 3, no. 2, 2014, Art. no. 1440001.
[10] B. Dober *et al.*, "Optical demonstration of THz, dual-polarization sensitive microwave kinetic inductance detectors," *J. Low Temp. Phys.*, vol. 184, no. 1/2, pp. 173–179, 2016.
[11] M. H. Abitbol *et al.*, *CMB-S4 Technology Book*, 1st ed., pp. 1–191, 2017. [Online]. Available: https://arxiv.org/abs/1706.02464
[12] A. Murphy *et al.*, "Multi-mode horn design and beam characteristics for the Planck satellite," *J. Instrum.*, vol. 5, no. 4, 2010, Art. no. T04001.
[13] L. Novotny, M. Frimmer, and R. Reimann, "Angular spectrum representation," Lecture Notes in Nano-Optics, 2016. [Online]. Available: https://www.photonics.ethz.ch/fileadmin/user_upload/Courses/EM_Fi eldsAndWaves/AngularSpectrumRepresentation.pdf
[14] D. Teyssier *et al.*, "HIFI pre-launch calibration results," in *Proc. 19th Int. Symp. Space THz Technol.*, 2008, pp. 113–120.
[15] C. Y. E. Tong *et al.*, "Near field vector beam measurements at 1 THz," *IEEE Microw. Wireless Compon. Lett.*, vol. 13, no. 6, pp. 235–237, Jun. 2003.
[16] J. Tervo and J. Turunen, "Angular spectrum representation of partially coherent electromagnetic fields," *Opt. Commun.*, vol. 209, no. 1–3, pp. 7–16, 2002.
[17] M. Carter *et al.*, "Phase and amplitude antenna measurements on an sis mixer fitted with a double slot antenna for alma band 9," in *Proc. 13th Int. Symp. Space THz Technol.*, Mar. 2002, pp. 515–524.
[18] W. Jellema, "Optical design and performance verification of Herschel-HIFI," Ph.D. dissertation, Univ. Groningen, Groningen, The Netherlands, 2015.
[19] M. Naruse *et al.*, "Near-field beam pattern measurement of qualification model of ALMA band 8 (385–500 GHz) cartridge receiver," *Exp. Astron.*, vol. 24, no. 1–3, pp. 89–107, 2009.
[20] A. M. Baryshev *et al.*, "The alma band 9 receiver—Design, construction, characterization, and first light," *Astron. Astrophys.*, vol. 577, 2015, Art. no. A129.
[21] C. N. Thomas and S. Withington, "Optical modeling techniques for multimode horn-coupled power detectors for submillimeter and far-infrared astronomy," *J. Opt. Soc. Amer. A*, vol. 30, no. 8, pp. 1703–1713, 2013.
[22] K. K. Davis *et al.*, "Proof-of-concept demonstration of vector beam pattern measurements of kinetic inductance detectors," *IEEE THz Sci. Technol.*, vol. 7, no. 1, pp. 98–106, Jan. 2017.
[23] J. van Rantwijk *et al.*, "Multiplexed readout for 1000-pixel arrays of microwave kinetic inductance detectors," *IEEE Trans. Microw. Theory Techn.*, vol. 64, no. 6, pp. 1876–1883, Jun. 2016.
[24] L. Otal, "The optical system and the astronomical potential of A-MKID, a new camera using microwave kinetic inductance detectors," Ph.D. dissertation, Rheinischen Friedrich-Wilhelms-Universität Bonn, 2014. [Online]. Available: http://hss.ulb.uni-bonn.de/2015/4094/4094.pdf
[25] S. J. C. Yates *et al.*, "Surface wave control for large arrays of microwave kinetic inductance detectors," *IEEE THz Sci. Technol.*, vol. 7, no. 6, pp. 789–799, Nov. 2017.
[26] J. A. Murphy, "Distortion of a simple Gaussian beam on reflection from off-axis ellipsoidal mirrors," *Int. J. Infrared Millim. Waves*, vol. 8, no. 9, pp. 1165–1187, Sep. 1987.
[27] "GRASP," TICRA, 2017. [Online]. Available: http://www.ticra.com/products/software/grasp
[28] L. Ferrari, S. J. C. Yates, M. Eggens, A. M. Baryshev, and J. Baselmans, "MKID large format array testbed," *IEEE Trans. Terahertz Sci. Technol.*, vol. 8, no. 6, pp. 572–580, Nov. 2018, doi: 10.1109/TTHZ.2018.2871365.
[29] K. K. Davis *et al.*, "Analysis techniques for complex field radiation pattern measurements," *Proc. SPIE*, vol. 10708, pp. 10708–10715, 2018.
[30] J. A. Nelder and R. Mead, "A simplex method for function minimization," *Comput. J.*, vol. 7, no. 4, pp. 308–313, 1965.
[31] M. Calvo *et al.*, "Improved mm-wave photometry for kinetic inductance detectors," *Astron. Astrophys.*, vol. 551, 2013, Art. no. L12.
[32] L. Bisigello, S. J. C. Yates, V. Murugesan, J. J. A. Baselmans, and A. M. Baryshev, "Calibration scheme for large kinetic inductance detector arrays based on readout frequency response," *J. Low Temp. Phys.*, vol. 184, no. 1, pp. 161–166, 2016.
[33] H. A. Yousif and R. Melka, "Bessel function of the first kind with complex argument," *Comput. Phys. Commun.*, vol. 106, no. 3, pp. 199–206, 1997.
[34] S. Lea, "Solutions in cylindrical coordinates: Bessel functions," in *Course Lectures*, San Francisco State Univ., San Francisco, CA, USA, 2018. [Online]. Available: http://www.physics.sfsu.edu/˜lea/courses/grad/bessels.pdf
[35] D. W. Marquardt, "An algorithm for least-squares estimation of nonlinear parameters," *SIAM J. Appl. Math.*, vol. 11, no. 2, pp. 431–441, 1963.
[36] "CST microwave studio," Dassault Systems, 2016. [Online]. Available: https://www.cst.com/
[37] "Zemax optical studio," Zemax LLC, 2013. [Online]. Available: https://www.zemax.com/
[38] P. F. Goldsmith, *Quasioptical Systems: Gaussian Beam Quasioptical Propagation and Applications* (IEEE Press/Chapman & Hall Publishers Series on Microwave Technology and RF Quasioptical Systems). New York, NY, USA: Springer, 1998.
[39] P. C. Clemmow, *The Plane Wave Spectrum Representation of Electromagnetic Fields* (Electromagnetic Wave Theory). New York, NY, USA: Oxford Univ. Press, 1996.
[40] J. Ruze, "Antenna tolerance theory—A review," *Proc. IEEE*, vol. 54, no. 4, pp. 633–640, Apr. 1966.
[41] M. J. Griffin, J. J. Bock, and W. K. Gear, "Relative performance of filled and feedhorn-coupled focal-plane architectures," *Appl. Opt.*, vol. 41, no. 31, pp. 6543–6554, Nov. 2002.
[42] R. Tkadlec and Z. Nováček, "Radiation pattern reconstruction from the near-field amplitude measurement on two planes using PSO," *Radioengineering*, vol. 14, no. 4, pp. 63–67, 2005.
[43] M. J. M. van der Vorst *et al.*, "Effect of internal reflections on the radiation properties and input impedance of integrated lens antennas-comparison between theory and measurements," *IEEE Trans. Microw. Theory Techn.*, vol. 49, no. 6, pp. 1118–1125, Jun. 2001.

Authors' photographs and biographies not available at the time of publication.